PHOTONICS Research

Phase calibration for integrated optical phased arrays using artificial neural network with resolved phase ambiguity

LEMENG LENG,[1,2,3,4,†] ZHAOBANG ZENG,[1,2,3,4,†] GUIHAN WU,[1,2,3,4] ZHONGZHI LIN,[1,2,3,4] XIANG JI,[1,2,3,4] ZHIYUAN SHI,[1,2,3,4] AND WEI JIANG[1,2,3,4,*]

[1]*College of Engineering and Applied Sciences, Nanjing University, Nanjing 210093, China*
[2]*Key Laboratory of Intelligent Optical Sensing and Manipulation, Ministry of Education, Nanjing University, Nanjing 210093, China*
[3]*Jiangsu Key Laboratory of Artificial Functional Materials, Nanjing University, Nanjing 210093, China*
[4]*National Laboratory of Solid-State Microstructures, Nanjing 210093, China*
Corresponding author: weijiang@nju.edu.cn

Phase calibration for optical phased arrays (OPAs) is a key process to compensate for the phase deviation and retrieve the initial working state. Conventional calibration approaches based on iterative optimization algorithms are tedious and time-consuming. The essential difficulty of such a problem is to inversely solve for the phase error distribution among OPA elements from the far-field pattern of an OPA. Deep-learning-based technology might offer an alternative approach without explicitly knowing the inverse solution. However, we find that the phase ambiguities, including conjugate ambiguity and periodic ambiguity, severely deter the accuracy and efficacy of deep-learning-based calibration. Device-physics-based analysis reveals the causes of the phase ambiguities, which can be resolved by creating a tailored artificial neural network with phase-masked far-field patterns in a conjugate pair and constructing a periodic continuity-preserving loss function. Through the ambiguity-resolved neural network, we can extract phase error distribution in an OPA and calibrate the device in a rapid, noniterative manner from the measured far-field patterns. The proposed approach is experimentally verified. Pure main-beam profiles with >12 dB sidelobe suppression ratios are observed. This approach can help overcome a crucial bottleneck for the further advance of OPAs in a variety of applications such as lidar.   © 2022 Chinese Laser Press

https://doi.org/10.1364/PRJ.435766

1. INTRODUCTION

Integrated optical phased arrays (OPAs) can control the propagating behavior of light in free space without bulky mechanical components, showing great potential in applications such as light detection and ranging (lidar), wireless optical communication, and image projection [1–24]. Owing to the complementary metal oxide semiconductor-compatible (CMOS) processes, a large number of components can be readily integrated on-chip, forming a compact phased array system. The optical paths of the elements of an integrated OPA are generally designed with fan-in waveguides to form an aligned wavefront as an initial state [1–3]. However, the high index contrast of silicon waveguides always results in substantial random phase errors in the paths of the waveguides due to fabrication variation, which generates a distorted far-field pattern different from the ideal initial state. These fabrication-induced phase errors are generally compensated for by adding an extra phase shift determined from optimal searching methods such as the particle swarm optimization (PSO) algorithm, gradient descent

algorithm, and genetic algorithm [12–23]. Such an iterative, optimization-based calibration process is able to align the wavefront and to achieve reasonably good results in practice. However, the phase calibration process is always time-consuming. Recently, encouraging improvements of the calibration accuracy and efficiency have been demonstrated by modifying the algorithm, using an on-chip monitor or interference-assisted setup [24–27], although the core algorithms remain based on an iterative search of the optimum in a high-dimensional space. For a large number of OPA device samples that are needed in real applications, the lengthy iteration process needs to be repeated for each sample, which can result in prohibitive time and cost for calibration [for an illustrative example, see Appendix D, Fig. 10(c)].

For an OPA, it would be desirable to identify the phase error distribution among the OPA elements from the irregular far-field pattern instantly and calibrate the device to an ideal initial state without prolonged iterative processes. However, it is difficult to inversely solve the complex nonlinear relationship

between the far-field pattern and near-field phase distribution to find the phase errors in such a photonic system. Recently, the artificial neural network (ANN) has provided new solutions for many subjects such as nanophotonic designs [28], identifying the different phases of matter [29], and solving ellipsometric problems [30]. Its ability to deal with complex nonlinear mapping makes it an ideal building block of a framework to solve the inverse problem for OPA calibration. In this work, we demonstrate an ANN-assisted method to identify the phase error distribution among OPA elements and calibrate an OPA. As we shall see, phase ambiguity is a pivotal problem in the OPA system that may prevent the efficacy of the ANN. Device-physics analysis of the OPA can offer insight to overcome ambiguity-induced problems. Combining the ANN and OPA device-physics analysis, we experimentally demonstrate a rapid, iteration-free calibration approach.

2. ANN FOR OPA CALIBRATION

The devices we propose to calibrate are designed and fabricated on a silicon-on-insulator (SOI) wafer. Figure 1(a) schematically shows the OPA consisting of a grating coupler for input coupling, multimode interferences (MMIs) tree for power splitting, thermo-optic phase shifters, and a dense output waveguide array (see details in Appendix A). The operation wavelength is set to be $\lambda = 1550$ nm. There are $N - 1$ phase shifters in this device to control the relative phase of elements #2–#N. The first element is considered as a reference channel, to exploit the freedom of setting a reference phase. Hence, the output phase error distribution of N elements is

$$\boldsymbol{\varphi} = [\varphi_1, \varphi_2, \varphi_3, ..., \varphi_{N-1}, \varphi_N],$$

where $\varphi_1 \equiv 0$.

The relative phase error distributions are ubiquitous and unpredictable on different devices fabricated in a batch. For the integrated waveguides, fabrication-induced phase errors (e.g., due to random fluctuations of the waveguide widths and hence propagation constants) accumulate along the propagation lengths of waveguides, which is unavoidable. Other possible contributions to phase errors are discussed in Appendix A. The total phase errors need to be treated. Note that the far-field beam profile remains unchanged for any phase φ_m to change by a multiple of 2π. Hence, we only need to consider the phase error of each element in the range of $[0, 2\pi]$. To align the wavefront for all elements, we first build an ANN model to identify the phase errors from the unordered far-field patterns directly. We generate the data set according to the phased array theory [31]. The normalized far-field intensity pattern $I(\boldsymbol{\varphi}, \theta)$ of the

N-element phased array can be calculated using the following equations:

$$I(\boldsymbol{\varphi}, \theta) = \text{Nor}\{S(\theta)|E(\boldsymbol{\varphi}, \theta)|^2\}, \tag{1}$$

$$E(\boldsymbol{\varphi}, \theta) = \sum_{m=1}^{N} a_m \exp[-j(\sigma_m + \varphi_m)], \tag{2}$$

$$\sigma_m = -2\pi d_m \sin\theta/\lambda, \tag{3}$$

where $E(\boldsymbol{\varphi}, \theta)$ indicates the array-dependent far-field wave amplitude variation at far-field angle θ, which depends on phase error distribution $\boldsymbol{\varphi}$. Nor$\{\cdot\}$ indicates the normalization operation for unity peak intensity, a_m is the emitting amplitude of the mth element, σ_m indicates the phase offset depending on radiation direction, and d_m is the position of the center of the element #m in reference to the center of the emitter array. $S(\theta)$ is the far-field envelope, where θ is the far-field angle ranging from $-90°$ to $90°$. As elements of OPA usually carry equal optical power, we can let $a_m = a_1$ (which can conveniently be set to unity). Figure 2(a) shows an example of random phase error distribution among different waveguides (the red lines in the waveguides indicate locations where phase equals $2m\pi$), and the generated far-field profile.

Then we build the Net 1, as shown in Fig. 2(c). The sizes of the input and output layers are N_θ and $N - 1$, respectively, corresponding to the number of points in the far-field patterns and the relative phase errors of elements #2–#N, as shown in Fig. 2(a). The input layer with N_θ neurons and h hidden layers, each with $M_1, M_2, ..., M_h$ neurons, are connected with a sigmoid activation function to build a forward-propagated neural network. Here h represents the total number of the hidden layers. We also use a sigmoid function to normalize the output in range of [0, 1]. The predicted phase errors can be recovered by multiplying the output by 2π. A loss function of mean square error (MSE) between the predicted phase errors and the real phase errors is selected to train the model, which is defined as

$$\text{loss(MSE)} = \sum_{m=2}^{N} (\varphi_m - \tilde{\varphi}_m)^2/(N-1), \tag{4}$$

where φ_m and $\tilde{\varphi}_m$ are, respectively, the predicted phase error and the real phase error of element #m. The network is implemented with the Google TensorFlow 2.0 platform using a single NVIDIA GeForce GTX 1050 GPU with 4 GB RAM. For a proof-of-concept demonstration, we set N_θ, M_1, M_2, M_3, and $N - 1$ as 361, 1000, 800, 200, and 15 (three hidden layers M_1, M_2, M_3 are used, N_θ corresponds to the input layer, and $N - 1$ corresponds to the output layer). The principle demonstrated here is applicable to an OPA of any size. For this case, we generate 10,000 far-field patterns labeled with the corresponding phase errors to train the Net 1. Adam optimizer with an initial learning rate of 0.001 is used to update the weight and bias for the total neurons during backpropagation. During training, the generated data set is divided into the training set and the validation set in an 85%/15% ratio. A checkpoint for the best parameter recording and halved learning rate is used for every 500 epochs.
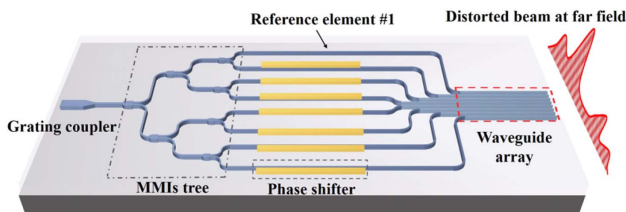

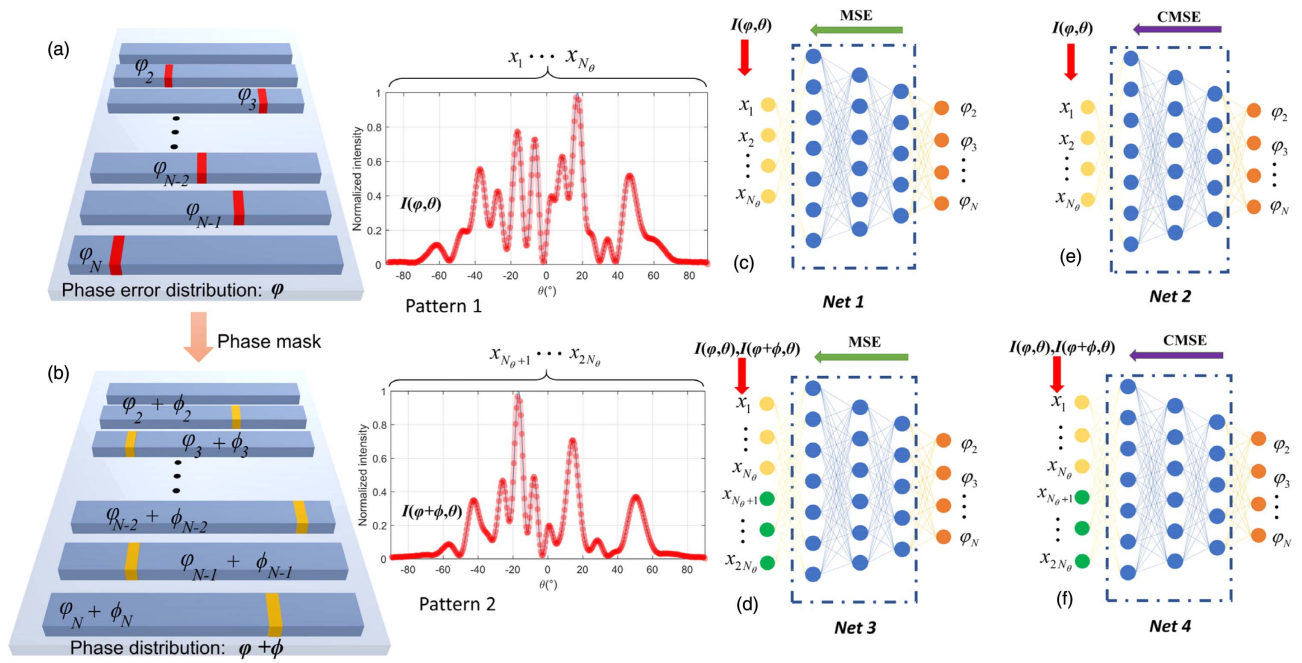**Fig. 1.** Schematic view of an integrated OPA, along with the far-field pattern.

Fig. 2. Example of the far-field patterns for feeding the neural network, $I(\boldsymbol{\varphi}, \theta)$ and $I(\boldsymbol{\varphi} + \boldsymbol{\phi}, \theta)$, generated by the OPA with (a) phase error of $\boldsymbol{\varphi}$ and (b) additional phase mask of $\boldsymbol{\phi}$. (c)–(f) Build ANNs with different architectures. The green and purple arrows indicate the backpropagation of the ANNs using a loss function of MSE or CMSE. The red arrows indicate the configurations of the data for input [using pattern 1, $I(\boldsymbol{\varphi}, \theta)$, with N_θ data points or the combination of pattern 1 and pattern 2, $I(\boldsymbol{\varphi}, \theta), I(\boldsymbol{\varphi} + \boldsymbol{\phi}, \theta)$, with $2N_\theta$ data points].

3. RESOLVE AMBIGUITY IN THE ANN MODEL OF AN OPA

Training loss and validation loss of the Net 1 cannot achieve convergence to a small value after 2500 epochs, as shown in Fig. 3(a). OPA-oriented device-physics analysis shows that this is caused by the phase ambiguity in the OPA cast into the ANN model. The ANN model is trained to build a functional relationship between the input and output layers, which in principle requires a one-to-one mapping. As presented by
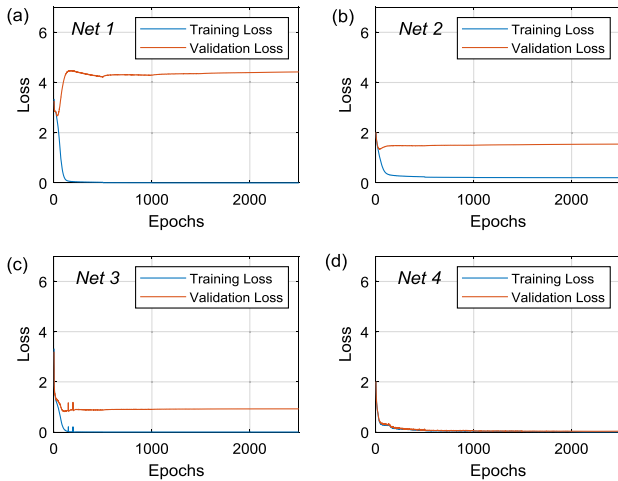

Fig. 3. Loss of (a) Net 1, (b) Net 2, (c) Net 3, and (d) Net 4 with the architecture in Figs. 2(c)–2(f) evolving with training epochs. Red curves indicate loss of the training set, and blue curves indicate loss of the validation set.

Eqs. (1)–(4), the far-field pattern of the OPA mainly depends on the phase error distribution of $\boldsymbol{\varphi}$. However, considering another conjugate phase error distribution of $\boldsymbol{\varphi}' = -[\varphi_N, \ldots, \varphi_2, \varphi_1]$, the corresponding $E(\boldsymbol{\varphi}', \theta)$ is given by

$$E(\boldsymbol{\varphi}', \theta) = \sum_{m=1}^{N} \exp[-j(\sigma_m - \varphi_{N-m+1})]. \tag{5}$$

Due to the symmetric position d_m of the waveguide-based emitters ($d_m = -d_{N-m+1}$), σ_m equals $-\sigma_{N-m+1}$, based on Eq. (3). Hence $E(\boldsymbol{\varphi}', \theta)$ can be written as

$$E(\boldsymbol{\varphi}', \theta) = \sum_{m=1}^{N} \exp[j(\sigma_m + \varphi_m)]. \tag{6}$$

Comparing Eqs. (2) and (6), magnitudes of $|E(\boldsymbol{\varphi})|$ and $|E(\boldsymbol{\varphi}')|$ are totally identical at the far field, since $E(\boldsymbol{\varphi}) = E(\boldsymbol{\varphi}')^*$. Consequently, the Net 1 cannot find the right direction between two conjugate cases to minimize the loss, and then build an inaccurate mapping from far-field patterns to the phase labels in the data set during training. In this case, the ANN output phase error distribution will be some sort of "intermediate state" between two conjugate distributions. As these two conjugate cases ($\boldsymbol{\varphi}$ and $\boldsymbol{\varphi}'$) reverse their spatial orders of error sequence and change the signs, their distance in the N-dimensional phase error distribution space is usually fairly large. Thus, the "intermediate state" given by the ANN output (the "interpretation" of "intermediate" is network-dependent) is likely far from either $\boldsymbol{\varphi}$ or $\boldsymbol{\varphi}'$. One can readily see from Eqs. (1)–(3) that the OPA beam profiles calibrated by $\boldsymbol{\varphi}$,

φ', or their intermediate state will generally differ drastically also.

In order to resolve ambiguity caused by the conjugate phase distribution, we introduce an additive pattern 2, $I(\varphi + \phi, \theta)$, by tuning the phase shifters of element with a virtual phase mask of $\phi = [-\pi, 0, 0, \ldots, 0, 0]$ on top of the intrinsic relative random phase error distribution, as shown in Fig. 2(b). The additive pattern, $I(\varphi + \phi, \theta)$, can be calculated by

$$I(\varphi + \phi, \theta) = \text{Nor}\{S(\theta)|E(\varphi + \phi, \theta)|^2\}, \qquad (7)$$

where $E(\varphi + \phi, \theta)$ is given by

$$E(\varphi + \phi, \theta) = \exp[-j(\sigma_1 + \varphi_1 - \pi)] + \exp[-j(\sigma_N + \varphi_N)]$$
$$+ \sum_{m=2}^{N-1} \exp[-j(\sigma_m + \varphi_m)]. \qquad (8)$$

For the conjugate phase error distribution, $E(\varphi' + \phi, \theta)$ in Eq. (8) is given by

$$E(\varphi' + \phi, \theta) = \exp[j(\sigma_1 + \varphi_1)] + \exp[j(\sigma_N + \varphi_N + \pi)]$$
$$+ \sum_{m=2}^{N-1} \exp[j(\sigma_m + \varphi_m)]. \qquad (9)$$

Comparing Eqs. (8) and (9), $E(\varphi + \phi)$ and $E(\varphi' + \phi)$ are evidently different. Based on the analysis above, the combined far-field intensity patterns in a conjugate pair, $[I(\varphi, \theta), I(\varphi + \phi, \theta)]$, provide more features for the ANN to resolve the corresponding phase label, φ, from the ambiguous label φ'. Note that there is no phase shifter in element #1 for which we use an equivalent phase mask as $\phi = [0, \pi, \pi, \ldots, \pi, \pi]$ to achieve the same effect. Figure 2(b) shows a sample of input data generated by using the phase mask ϕ with N_θ data points.

Meanwhile, the output for such an optical system is a periodic function of phase, which is intractable for a standard neural network with a fixed output range, e.g., $[0, 2\pi)$. For instance, consider whether one of the actual phase errors φ_m is $2\pi - 0.001$. Within the computing/training accuracy, the network may find both $\varphi_{m,0} = 2\pi - 0.001$ and $\varphi'_{m,0} = 0$ correspond to roughly the same beam pattern according to Eqs. (1)–(3). However, $\varphi_{m,0}$ and $\varphi'_{m,0}$ are very far on the φ_m axis, and the network believes that they must belong to two different states, which results in confusion. Fundamentally, the intrinsic continuity of the mapping function at the two ends of this interval $[0, 2\pi)$ is lost, which can baffle the otherwise obvious convergence. To resolve such periodic ambiguity while retaining the intrinsic continuity, we transform the real phase errors, φ_m, and the predicted errors, $\tilde{\varphi}_m$, into the complex domain by defining

$$z_m = \exp(j\varphi_m), \quad \bar{z}_m = \exp(j\tilde{\varphi}_m). \qquad (10)$$

Then the continuity-preserving loss function (via a certain form of complex mean square error, or CMSE) is written as

$$\text{loss(CMSE)} = \frac{\sum_{m=2}^{N}[\text{Re}(z_m - \bar{z}_m)^2 + \text{Im}(z_m - \bar{z}_m)^2]}{N - 1},$$
$$(11)$$

where Re and Im are the real and imaginary parts of the complex, respectively.

Then, we construct the Net 2, Net 3, and Net 4 in Figs. 2(d)–2(f) with different network architectures or loss functions to tackle the ambiguities. The architectures of Net 2 and Net 1 are identical, but we introduce the CMSE loss function for Net 2 to solve the periodic ambiguity only, as indicated by the purple arrow in Fig. 2(e). The sizes of the hidden layers and output layers of Net 3 and Net 4 are identical with Net 1 and Net 2, respectively. The difference is that Net 3 and Net 4 use the combination of pattern1 and pattern 2 in Figs. 2(a) and 2(b) in conjugate pair to solve the conjugate ambiguity. The sizes of the input layers for these two nets increase to $2N_\theta$, as illustrated with different colors in Figs. 2(d) and 2(f). Hence, Net 4 using CMSE can solve both conjugate ambiguity and periodic ambiguity. It should be noted that the data set for ANN using the loss function, CMSE, is totally compatible with the one for ANN using a loss function of MSE. So, we train the Net 2 with the single-pattern data set the same as Net 1 (input dimension: $N_\theta = 361$). Net 3 and Net 4 are trained using same data set with an input dimension of $2N_\theta$ and output dimension of $N - 1$.

After training, the validation loss of Net 1 and Net 2 (single beam profile input) cannot achieve convergence. Meanwhile, when comparing the red curves in Figs. 3(a) and 3(c), MSE loss of Net 3 finally converges to a lower level (~ 0.92) than that of Net 1 using the loss function of MSE, indicating that the negative effect of the conjugate ambiguity during the training process has been eliminated. From Figs. 3(c) and 3(d), the periodic ambiguity is further removed. As shown in Fig. 3(d), the validation loss of Net 4 decreases to 0.04 (from >4 in Net 1), which indicates the high efficacy enabled by removing the conjugate ambiguity and periodic ambiguity. Here, the time for generating the two data sets (single-pattern and dual-pattern) is all below ~ 10 s. Additionally, due to the different complexity of the input layer, it takes about 2.5 h for Net 1 and Net 2 and about 3 h for Net 3 and Net 4 to complete the training process over 2500 epochs.

To further demonstrate the performance of the ANN models, we simulate far-field patterns before and after calibration according to the phase error distributions predicted by Net 1 to Net 4, using four arbitrary samples in the testing data set. Figures 4(a1)–4(a4) show the far-field patterns calculated by the phase error data in the four samples. The irregular far-field profiles in Figs. 4(b1)–4(b4) and 4(c1)–4(c4) illustrate that Net 1 and Net 2 cannot output valid phase distributions, due to the conjugate ambiguity. Meanwhile, the performance of Net 3 is better than we have expected, even if the validation loss after training is only around 0.9. It can still align the wavefront for the testing samples of ii) and iii) and form perfect beams pointed to 0° with side lobe suppression ratio (SLSR) of 12.29 dB and 12.75 dB, as shown in Figs. 4(d2) and 4(d3). However, the poor SLSRs in Figs. 4(d1) and 4(d4), caused by several incorrect elements, indicate the limited capability of MSE-based ANN. By analyzing the residual phase error data in the samples ii) and iii), Net 3 cannot accurately predict the phase of the elements which is close to 0 or 2π, which is consistent with our previous analysis on the periodic ambiguity. Finally, Figs. 4(e1)–(e4) present the beams calibrated by Net 4 with average SLSR of about 12.7 dB, showing the high
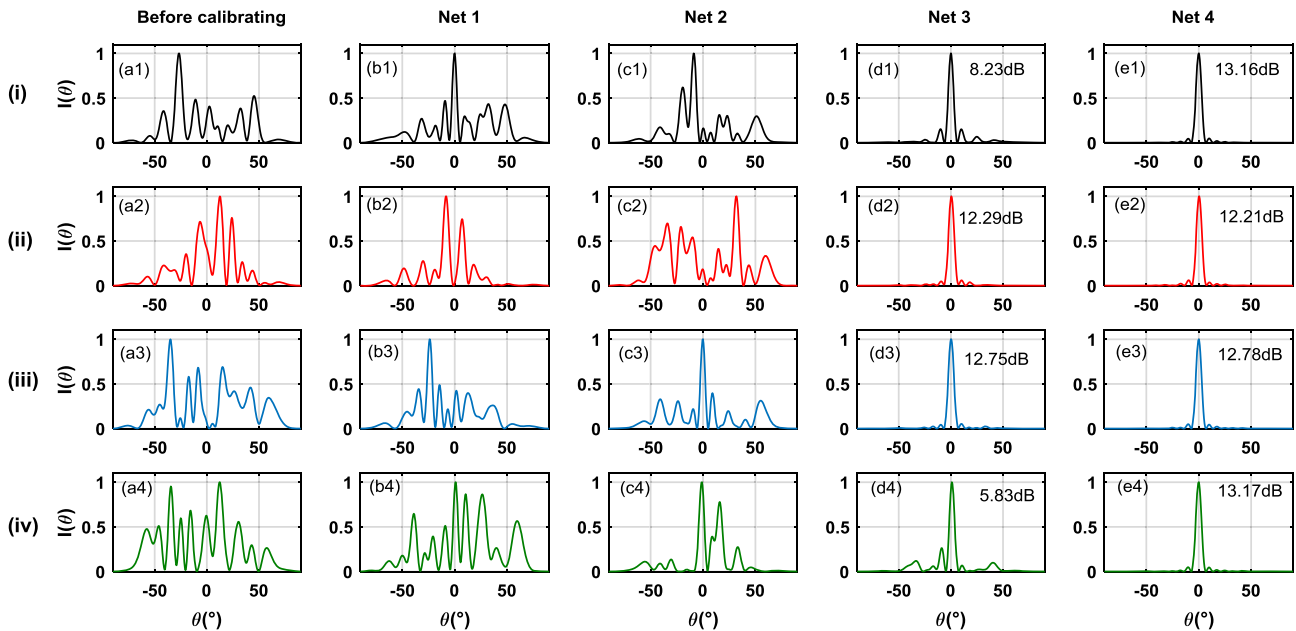
Fig. 4. Simulated performance of the ANNs using four randomly selected samples i) to iv) in testing set. Each sample is signified with a different color. (a1)–(a4) Far-field profiles before calibration. Beam profiles after calibration from the output of (b1)–(b4) Net 1; (c1)–(c4) Net 2; (d1)–(d4) Net 3; and (e1)–(e4) Net 4. The sidelobe levels of the formed beams are noted in (d1)–(d4) and (e1)–(e4). All figures share the same axis.

accuracy of Net 4 (see more detail in Fig. 8 in Appendix C), with both conjugate and periodic ambiguities resolved.

Hence, as we analyzed above, the enhanced training data set using far-field patterns in a conjugate pair and continuity-preserving loss function are indispensable elements for building such an ANN for phase calibration. It is important to point out that the elimination of symmetrical-array-induced conjugate ambiguity is a crucial factor to construct the unique mapping between the input layer and output layer. And the loss function CMSE introduced here to deal with periodic ambiguity can significantly improve the network performance as a supplemental approach.

4. EXPERIMENT

Figure 5 shows the experimental setup for automatic phase calibration based on the well-trained ANN. The optical signal
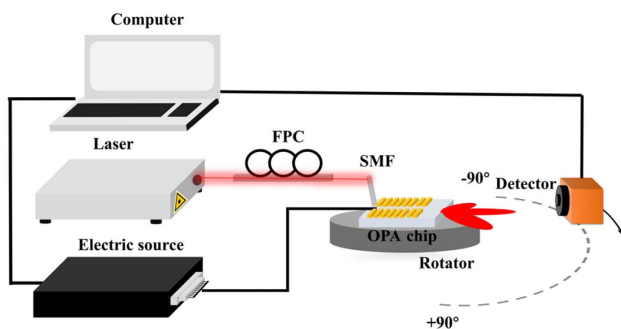

Fig. 5. Schematic of the experimental setup for automatic calibration via Net 4 (FPC, fiber polarization controller; SMF, single-mode fiber).

output from a 1550-nm laser is coupled to the grating coupler in the device by a single-mode fiber via a polarization controller. The far-field patterns are measured using a mechanically rotated detector, 10 cm away from the end face of the chip. During motion, the detector continuously samples the light intensity from –90° to +90°, and a far-field pattern is obtained and then transferred to the computer. A multichannel current source controlled by the computer provides driving power for the electrodes on the chip via 16 channel probes.

To verify the effectiveness of our approach, we arbitrarily chose two OPA devices fabricated on the same wafer to calibrate the mismatched wavefront. First, we measure the far-field pattern $I(\boldsymbol{\varphi}, \theta)$ without applying electric power to the phase shifters. Then we control the current source to uniformly apply a driving power of P_π to the phase shifters for the elements #2–#16 and obtain the far-field pattern $I(\boldsymbol{\varphi} + \boldsymbol{\phi}, \theta)$. Figure 7(b) in Appendix A shows the typical power-phase characteristic of the phase shifter as we vary the heating power. Once the far-field patterns in a conjugate pair are fed to the trained ANN model, it will predict the phase errors for each element. Then the computer automatically calculates the complementary heating power for calibrating the devices and then controls the electric source output driving current for each phase shifter to automatically align the wavefront.

The normalized far-field patterns in blue lines with multiple sidelobes in Figs. 6(a) and 6(d) are measured before calibration for the two devices, reflecting significant wavefront mismatch and variability in different dies. The red curves in Figs. 6(a) and 6(d) indicate the calculated beam profiles according to the phase error output from the ANN model. For device i), profiles of the highest and second-highest lobes in the measured far-field pattern at 0° and 49° are showing excellent agreement with the calculated pattern. Similar excellent agreement of the lobes
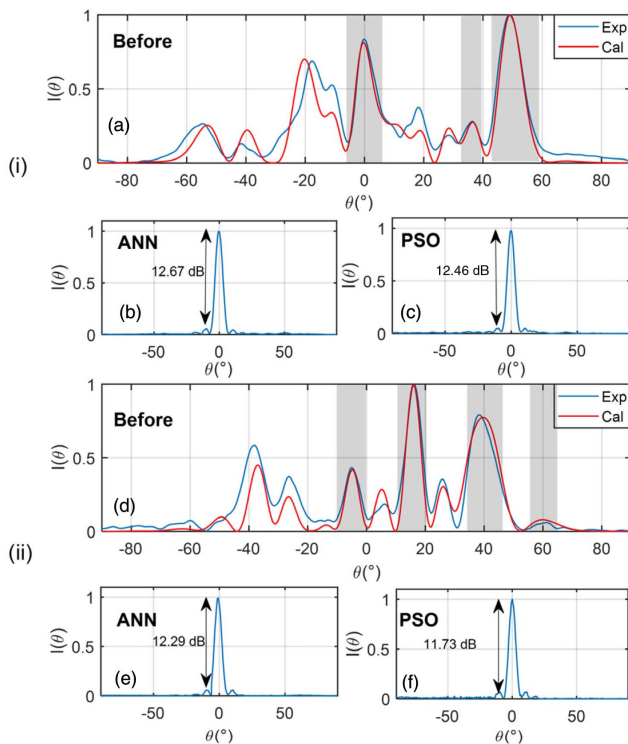
Fig. 6. Calibration for two arbitrarily selected devices i) and ii); experimentally measured far-field pattern before calibration (blue line) and calculated far-field pattern (red line) using the ANN-predicted phase error for (a) device i) and (d) device ii); measured beam profile after calibration using ANN for (b) device i) and (e) device ii); condensed beam profile after calibration using PSO for (c) device i) and (f) device ii).

at −5°, 16°, and 39° can also be observed from far-field patterns in device ii). In addition, positions of the measured lobes of lower levels are also in good agreement with the calculated patterns. Generally, this method ensures that the highest lobes agree well; the fairly small deviations in the lower lobes are due to potential small nonuniformities/noise (see discussion in Appendix C). Figures 6(b) and 6(e) show the measured beams of the two devices after calibration according to the phase error output from the ANN model, along with 12.67 and 12.29 dB SLSR in the entire field of view (180°). Figures 6(c) and 6(f) present the beams of the two devices using the PSO algorithm with 12.46 and 11.73 dB SLSR, which are in reasonable agreement with the ANN results.

5. DISCUSSION AND CONCLUSION

In terms of the calibration results, the beam profiles after calibration by PSO and ANN-assisted methods both show reasonable agreement with the simulation. But the ANN model is significantly more efficient in time than an iterative optimization approach such as the PSO. In this case, the PSO-based calibration roughly needs ∼100 iterations in experiment to achieve convergence with 200 far-field measurements per iteration (for 200 swarm elements), which is ∼20,000 measurements in total for one OPA device. Simulated statistics over 500 OPA devices show that the PSO approach can

achieve a moderate root-mean-square phase error (RMSE) ∼0.21π with ∼10^7 far-field measurements (see more detail in Appendix D). By comparison, this ANN-assisted method can instantly recognize the phase error distributions and calibrate the devices to achieve a relatively smaller phase error, RMSE < 0.04π (see Fig. 8 in Appendix C) in merely two far-field measurements per device, which is several orders of magnitude more efficient. Note that it is possible to reduce the number of iterations for the iterative optimal search approaches at the cost of calibration accuracy (or using nonevolutionary iterative search approaches at the cost of likelihood of approaching the global optimum). However, for the comparable calibration accuracy, this ANN-assisted approach is generally significantly more efficient. For a proof-of-principle demonstration, we use a 16-element 1D OPA here due to fabrication and test-equipment cost concerns. The principle demonstrated here can be readily applied to an OPA of any size, including 2D cases (OPAs of 1D or 2D share the same working principle). For a 2D OPA, one readily sees that both the conjugate ambiguity and periodic ambiguity occur similarly and can be treated similarly using the approaches shown here. For different OPA structures (or with a different number of elements), the ANN should be trained again with regenerated data sets. Note that while it takes some time to train the ANN, the calibration time per device is extremely short after training, and postcalibration performance variation is very small [see Fig. 10(b) in Appendix D]. Hence the ANN-based calibration is preferred in real-world applications where a large batch of OPA devices with the same design can be calibrated almost in real time with only one-time training of the ANN. For a proof-of-principle demonstration, we only use a sigmoid function, which performs well with the current ANN. If other network architectures (or different network depths) are used, other activation functions such as the rectified linear unit (ReLU) might be preferred [32]. As our ANN-assisted noniterative approach works for the full phase error range (0 – 2π), it may also be potentially useful in solving similar problems in related topics (e.g., Ref. [33]).

Note that many phase-retrieval techniques [34–36] have been developed with great success by considering the relation between the diffraction plane and image plane with spatial resolution of phase variation usually much larger than the wavelength. For the half-wavelength pitch OPA studied here, the spatial resolution of phase variation is a half-wavelength, and the corresponding radiation angles are far off the optical axis (up to 90°), which represents a regime seldom studied before in phase retrieval. Furthermore, OPA applications require a phase calibration metric of SLSR over the full field of 180°, which is seldom considered in phase retrieval. Also, in Eqs. (1)–(3), we have used a formalism not based on Fourier transform to deal with the special needs (far off-axis radiation) in our OPA calibration, whereas conventional phase retrieval usually uses Fourier transform. The phase diversity technique in phase retrieval uses a phase distortion to generate a second image for use together with the original image, for purposes such as combating image blurring [37,38]. Our approach to resolving the conjugate ambiguity appears similar to that technique in the aspect of taking more than one "imaging"

measurement (note: an "imaging" measurement is just a far-field measurement here). However, we theoretically reveal the exact need of one extra measurement for a different application—OPAs. For an OPA with radiation angles up to 90° (a regime seldom studied in phase retrieval), we have presented conjugate ambiguity analysis: proving the conjugate ambiguity resolution in OPAs needs exactly two imaging measurements. In contrast, three or more imaging measurements [38] may be needed in conventional phase retrieval for different reasons.

Deep learning (or neural networks) has also been introduced into phase retrieval and has shown great promise [39–41]. However, it has not altered the aspects of low spatial resolution of phase variation and small off-axis angles of conventional methods. Note that many common assumptions for routine phase retrieval need to be revised for subwavelength spatial resolution (or high spatial frequency, or far off-axis cases). Considering the nonlinearity in the problem, nontrivial efforts are needed to adapt conventional phase-retrieval methods to achieve the same efficiency and accuracy (judged by the SLSR metric for OPAs) in the regime of subwavelength spatial resolution. Note that many things that can be easily done at large scales can be extremely difficult at subwavelength scales.

In summary, we have demonstrated a noniterative phase calibration approach based on machine-learning technology for integrated OPAs. Thanks to device-physics-based analysis that helps resolve conjugate ambiguity and periodic ambiguity in phase, the well-trained ANN model is able to identify the phase error distributions and retrieve initial working state for the OPAs from merely two measurements of the far-field patterns. Compared with the iterative calibration methods, our neural-network-assisted approach is highly efficient, noniterative, and suitable for calibration of a massive set of device samples. As myriads of lidars are envisioned to be needed in future widespread deployment of self-driving cars, this work may potentially provide a key foundation for rapid, massive calibration of OPA devices with high-quality beam characteristics for widespread use of lidars.

APPENDIX A: DEVICE STRUCTURE, FABRICATION, AND TESTING

The OPA is fabricated on SOI wafers with 2 μm buried oxide and a 220 nm top silicon layer. Three steps of etching are utilized to fabricate the grating coupler, MMIs, and waveguides. The etched structure is then covered by a 3-μm-thick SiO_2 layer for surface protection and for isolating the optical waveguide from metal layers. A waveguide superlattice with an interwaveguide pitch of 0.8 μm is arranged periodically to form the emitters at the end face of the chip with cross talk below −20 dB [23]. A thin TiN layer is used to form the heaters in thermo-optical phase shifters. The TiN-based thermo-optic phase shifters are separated with a pitch of 50 μm to avoid thermal cross talk. Aluminum metal wires, via holes and electrode pads, are fabricated to conduct electric current to the phase shifters. The testing setup, including the laser, a multichannel electric current source, a detector, alignment stages, and other components, is carefully inspected and adjusted to ensure its proper functionality before phase calibration. Note that different waveguides in the OPA travel along paths with somewhat

different lengths to produce phase offsets between signals in different waveguides. In addition, the different widths of the waveguide superlattice not only suppress cross talk, but also produce phase offsets between different OPA elements due to their different propagation constants. Overall, these two effects produce deterministic phase errors (in contrast to random phase errors due to fabrication variation). The approach in this work is applicable to the total phase errors of any combination (random or deterministic) regardless of their origins. Note that the waveguide superlattice-induced effect in far-field beam characteristics has been minimized so that the beam can be treated nearly as from a uniform OPA. Small residual effects due to the superlattice in the context of calibration are discussed in subsequent Appendix C. Due to the subwavelength pitch of this OPA, direct measurement of the near-field phase variation with half-wavelength resolution is difficult. The near-field (phase) imaging techniques used in the case of large pitch OPAs (e.g., Refs. [27,42]) cannot offer subwavelength resolutions due to insufficient numerical apertures of lenses.

Note that OPAs with an emitter pitch larger than a half-wavelength (e.g., some OPAs with grating emitters) will generate strong grating lobes at the far field. In practice, such OPAs generally work only in the range of $-\arcsin(\lambda/2d)$ and $\arcsin(\lambda/2d)$, where the strong grating lobes are absent. As the input angular pattern to the ANN is limited to this range with no strong grating lobes, our approach can be readily adapted to such OPAs in practice. It is well known the far-field pattern outside this range can be deterministically related to the pattern in this range; hence, the pattern in this range should contain sufficient information to solve for the phase deviation.

APPENDIX B: SUPPORTING EXPERIMENTAL DATA FOR SINGLE-CHANNEL PHASE CHARACTERISTICS

Before calibration, we first measure resistance of the elements #2–#16 through multipin probes for the tested device #1, shown in Fig. 7(a). The resistance of the phase shifter slightly fluctuates around 510 Ω, showing the good uniformity of the heaters, which enables us to obtain the additive far-field pattern by synchronously tuning the elements #2–#16 with π phase shift.

Then, phase versus heating power relationship for the thermo-optic phase shifter of the OPA is obtained by embedding an identical phase shifter in one arm of an integrated Mach–Zehnder interferometer (as in a thermo-optic switch) fabricated together with the OPA. The output intensity versus
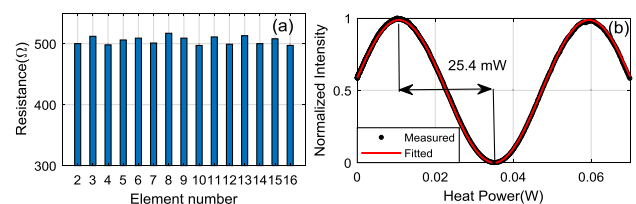

Fig. 7. (a) Measured resistances of the phase shifters in our 16-channel OPA; (b) measured (scatter) and fitted (line) heating power versus output intensity for the phase shifter embedded in an interferometer.

heating power relation of the switch, along with the fitted sinusoidal curve, as shown in Fig. 7(b), confirms a linear phase shift versus a heating-power relation. Based on the linear functional relationship between the applied electric power and phase shift, the ANN-predicted phase errors can be converted to compensating the electric power for each channel.

APPENDIX C: ACCURACY AND ROBUSTNESS OF THE NETWORK

For the ANN we present in Fig. 2(f), the continuity-preserving loss function in Eq. (11) is used to solve the periodic ambiguity. Based on this concept, we define the predicted accuracy for a single sample in the testing set by

$$S = \frac{1}{N-1} \sum_{i=2}^{N} \psi_i, \tag{C1}$$

where N is the number of elements of the OPA, ψ_i measures the angular deviation of the element #i and is given by

$$\psi_i = 2 \arcsin \frac{|\exp(j\varphi_i) - \exp(j\tilde{\varphi}_i)|}{2}, \tag{C2}$$

where φ_i and $\tilde{\varphi}_i$ are the real phase error and predicted phase error of the element #i, respectively. In Fig. 8, we present the distribution of calculated S, using $M = 500$ groups of testing data. The RMSE is given by

$$\mathrm{RMSE}(S) = \sqrt{\sum_{j=1}^{M} S_j^2 / M}. \tag{C3}$$

The experimentally measured far-field patterns for ANN input could slightly deviate from the theoretically generated data. Such small deviations will affect the network performance in practice. For our devices and experiment setup, there are three effects that would cause such deviations. First, the small nonuniformity of the phase shifter, as we discussed above, will mainly affect the measured additive pattern (used for ANN input). Second, due to the design of the waveguide superlattice, propagation loss varies with the waveguide width and will slightly affect the optical power uniformity of the emitters [23]. And finally, the noise at the detector end also affects the measured far-field patterns. Thus, we investigate the robustness of the ANN model based on the analysis above.
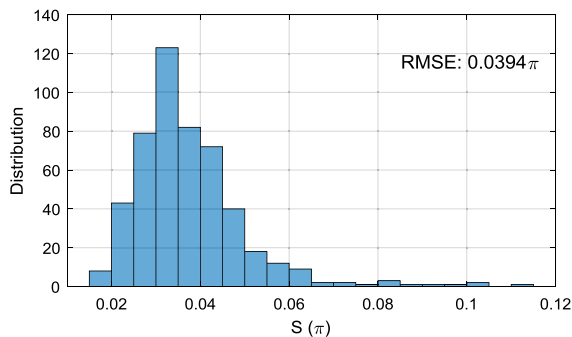
Fig. 8.   Distribution of calculated S with 500 samples in testing set.
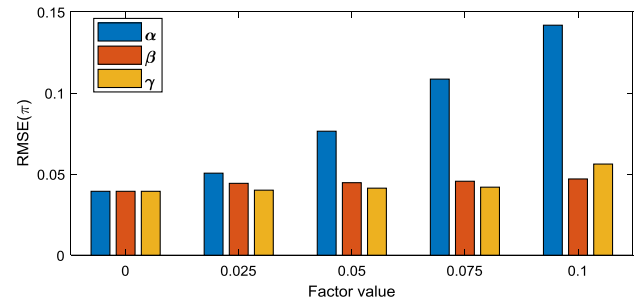
Fig. 9.   Accuracy of the ANN versus α, β, and γ.

To simulate the phase-shifter nonuniformity at different levels, the phase mask for generating the additive pattern, $\boldsymbol{\phi} = [0, \pi, \pi, \ldots, \pi, \pi]$, is multiplied by $1 + \alpha g_1$, where g_1 is the random number generated from a standard normal distribution in the range of [–1, 1], and α is the nonuniformity level. We simulate the optical power nonuniformity using nonuniformity level β. The optical power distribution is multiplied by $1 - \beta g_2$, where g_2 is the random number generated from a standard normal distribution in the range of [0, 1]. Similarly, the generated far-field patterns in the test data are multiplied by $1 - \gamma g_3$ to simulate the noise at the detector end. We consider the case of γ up to 0.1 here. Note that the superlattice may induce very weak superlattice lobes with small magnitude <0.01 (< -20 dB) [23], which can be effectively counted into the noise at the detector end (i.e., contributing 0.01 into γ) and obviously has little effect on calibration compared to other effects (total γ up to 0.1) we consider.

As we demonstrated in Fig. 9, the accuracy of the ANN is more sensitive to the phase-shifter nonuniformity level α. In our device, the fluctuation of the measured resistance of the phase shifters is about $\pm 2\%$, corresponding to the $\alpha = 0.02$. Packaged devices by wire bonding can suppress fluctuation to $\pm 1\%$ and will improve the calibration accuracy in practice [2]. Meanwhile, the nonuniformity in optical power distribution and the noise at the detector end have relatively small impact on performance. Such nonuniformity effects may occur synchronously to affect accuracy; fine-tuning of each channel is used at the end to check and minimize potential small deviation of the calibrated beam from the intended optimal state caused by the above nonuniformities. Note that the fine-tuning is also needed at the end of the PSO-assisted calibration to check each channel for eliminating the potential local optimum.

APPENDIX D: CALIBRATION EFFICIENCY OF THE PSO AND ANN

In order to illustrate the time efficiency of our noniterative method, we simulate the calibration process using PSO with 500 OPA devices in the test data set. Actually, the performance of the PSO algorithm is mostly dependent on the swarm size (number of elements in the swarm). Figure 10(a) presents the calculated RMSE of the samples in the test set with different swarm sizes after 100 iterations. It confirms that the PSO using sufficiently large swarm sizes can escape local optimum and converges to a good result [43]. However, as we plotted in

Fig. 10(c), a large number of the swarm elements also require a huge number of experimental evaluations for calibration. Note that each experimental evaluation here requires one far-field measurement (including the process of reconfiguring the thermo-optic phase-shifters with a new set of driving current/voltage values). As an example, a PSO with 200 swarm elements needs 20,000 (200 × 100) evaluations for a single sample. [If 500 device samples need calibration, 1×10^7 evaluations in total are needed (200 × 100 × 500).] In practice, due to the large statistical variation of the PSO method (see error bars in Fig. 10(b)], sometimes the outcome after 100 iterations may be substantially below the expected value [i.e., below the mean sidelobe suppression values in Fig. 10(b)]. This reflects a local optimum quite far from the global optimum. Then one may have to restart the PSO calibration with a new set of initial "particles" for another round of 100 iterations or even more, which will take even more time. Note that every evaluation requires reconfiguring the thermo-optic phase-shifter arrays and experimental measurement of the OPA far-field intensity (both taking nonnegligible amount of time, typically on the order of 0.1 s or above), such that the total time cost for the large number of evaluations shown in Fig. 10(c) can be unbearable. Note that simulations show that the number of evaluations in an iterative calibration process can potentially be reduced by 1 or 2 orders of magnitude with a smart optimizing
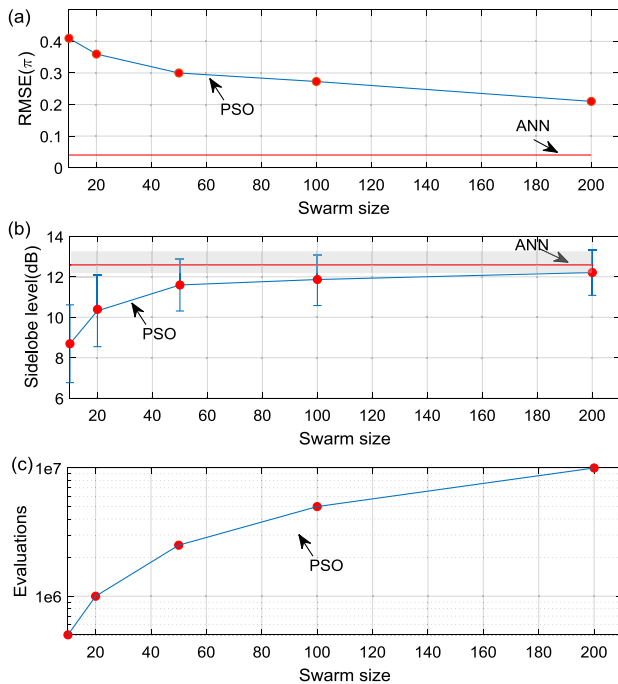

Fig. 11. Measured 2D beam profiles (a) before calibration, (b) after calibration using ANN, and (c) after calibration using PSO for device i) in Fig. 6.

algorithm [25], but the path of further reducing the number of evaluations significantly to the level achieved in this work remains unclear.

For comparison, for our ANN-assisted calibration method, the calibration accuracy (RMSE = 0.0394π) in Fig. 8 is better than the average PSO result with up to 200 swarm elements (RMSE = 0.21π) after 100 iterations. Meanwhile, our method does not need 100 iterations for each device sample; the time efficacy can be significantly improved by several orders of magnitude. To compare the performance of PSO and ANN by the sidelobe suppression ratio, we show the simulated statistics in Fig. 10(b). Compared to the best PSO performance, the ANN produces a comparable (slightly better) average sidelobe suppression ratio and smaller standard deviations, which is desirable.

APPENDIX E: BEAM CHARACTERISTIC OF THE END-FIRE OPA

Note that the current OPA in an end-fire configuration forms line-like beams extending vertically at the far field. Figure 11 shows the representative 2D profiles of the beams measured using a commercial infrared camera. Figures 11(a)–11(c) correspond to the beam profiles of the device i) in Fig. 6 before and after calibration in 44° × 34° field of view (limited by measurement equipment). One can see that the measured 2D beam patterns extend uniformly in the vertical direction, as expected for a line beam. In the horizontal direction, the precalibration beam profile in Fig. 11(a) shows irregular intensity variation, and the profiles in Figs. 11(b) and 11(c) after calibration with ANN and PSO approaches show only a clean beam in the middle. The horizontal profiles in Figs. 11(a)–11(c) are in good agreement with the 1D beam profiles in Figs. 6(a)–6(c) in the horizontal angular range of −22° to 22°.

Disclosures. The authors declare that there is no conflict of interest.

Data Availability. Data underlying the results presented in this paper are not publicly available at this time but may be obtained from the authors upon reasonable request.

†These authors contributed equally to this paper.

Fig. 10. Simulated PSO-based calibration statistics for 500 OPA devices, compared with ANN-model test results. (a) Simulated accuracy of the test set using PSO algorithms with different swarm sizes (the accuracy of ANN is marked for comparison); (b) simulated sidelobe suppression ratio statistics (the average and very small standard deviation of ANN are marked by a red line and a narrow shaded stripe, respectively); (c) total number of experimental evaluations (equivalent to the number of far-field measurements) required for this iterative method for 500 OPA devices. Note that the y axis is plotted using a logarithmic scale.
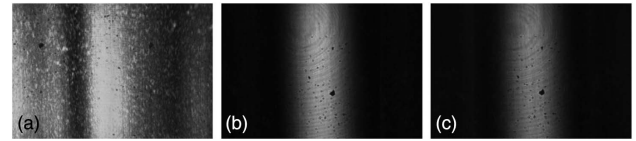
REFERENCES

1. K. Van Acoleyen, W. Bogaerts, J. Jágerská, N. Le Thomas, R. Houdré, and R. Baets, "Off-chip beam steering with a one-dimensional optical phased array on silicon-on-insulator," Opt. Lett. **34**, 1477–1479 (2009).

2. D. Kwong, A. Hosseini, Y. Zhang, and R. T. Chen, "1 × 12 unequally spaced waveguide array for actively tuned optical phased array on a silicon nanomembrane," Appl. Phys. Lett. **99**, 051104 (2011).

3. D. Kwong, A. Hosseini, J. Covey, Y. Zhang, X. Xu, H. Subbaraman, and R. T. Chen, "On-chip silicon optical phased array for two-dimensional beam steering," Opt. Lett. **39**, 941–944 (2014).

4. C. T. DeRose, R. D. Kekatpure, D. C. Trotter, A. Starbuck, J. R. Wendt, A. Yaacobi, M. R. Watts, U. Chettiar, N. Engheta, and P. S. Davids, "Electronically controlled optical beam-steering by an active phased array of metallic nanoantennas," Opt. Express **21**, 5198–5208 (2013).

5. J. Sun, E. Timurdogan, A. Yaacobi, E. S. Hosseini, and M. R. Watts, "Large-scale nanophotonic phased array," Nature **493**, 195–199 (2013).

6. W. Ke, N. Ampalavanapillai, L. Christina, W. Elaine, A. Kamal, L. Hongtao, and S. Efstratios, "High-speed indoor optical wireless communication system employing a silicon integrated photonic circuit," Opt. Lett. **43**, 1323–1326 (2018).

7. J. Midkiff, K. M. Yoo, J.-D. Shin, H. Dalir, M. Teimourpour, and R. T. Chen, "Optical phased array beam steering in the mid-infrared on an InP-based platform," Optica **7**, 1544–1547 (2020).

8. P. Wang, A. Kazemian, X. Zeng, Y. Zhuang, and Y. Yi, "Optimization of aperiodic 3D optical phased arrays based on multilayer Si₃N₄/SiO₂ platforms," Appl. Opt. **60**, 484–491 (2021).

9. H. Ito, Y. Kusunoki, J. Maeda, D. Akiyama, N. Kodama, H. Abe, R. Tetsuya, and T. Baba, "Wide beam steering by slow-light waveguide gratings and a prism lens," Optica **7**, 47–52 (2020).

10. N. Dostart, B. Zhang, A. Khilo, M. Brand, K. A. Qubaisi, D. Onural, D. Feldkhun, K. H. Wagner, and M. A. Popovi, "Serpentine optical phased arrays for scalable integrated photonic LIDAR beam steering," Optica **7**, 726–733 (2020).

11. W. Song, R. Gatdula, S. Abbaslou, M. Lu, A. Stein, Y. C. Lai, J. Provine, R. F. W. Pease, D. N. Christodoulides, and W. Jiang, "High-density waveguide superlattices with low crosstalk," Nat. Commun. **6**, 7027 (2015).

12. J. C. Hulme, J. K. Doylend, M. J. R. Heck, J. D. Peters, M. L. Davenport, J. T. Bovington, L. A. Coldren, and J. E. Bowers, "Fully integrated hybrid silicon two dimensional beam scanner," Opt. Express **23**, 5861–5874 (2015).

13. C. V. Poulton, M. J. Byrd, P. Russo, E. Timurdogan, M. Khandaker, D. Vermeulen, and M. R. Watts, "Long-range LiDAR and free-space data communication with high-performance optical phased arrays," IEEE J. Sel. Top. Quantum Electron. **25**, 7700108 (2019).

14. F. Aflatouni, B. Abiri, A. Rekhi, and A. Hajimiri, "Nanophotonic projection system," Opt. Express **23**, 21012–21022 (2015).

15. C. T. Phare, M. Shin, S. A. Miller, B. Stern, and M. Lipson, "Silicon optical phased array with high-efficiency beam formation over 180 degree field of view," arXiv:1802.04624 (2018).

16. J. K. Doylend, M. J. R. Heck, J. T. Bovington, J. D. Peters, L. A. Coldren, and J. E. Bowers, "Two-dimensional free-space beam steering with an optical phased array on silicon-on-insulator," Opt. Express **19**, 21595–21604 (2011).

17. Y. Zhang, Y.-C. Ling, K. Zhang, C. Gentry, D. Sadighi, G. Whaley, J. Colosimo, P. Suni, and S. J. Ben Yoo, "Sub-wavelength-pitch silicon-photonic optical phased array for large field-of-regard coherent optical beam steering," Opt. Express **27**, 1929–1940 (2019).

18. S. A. Miller, Y.-C. Chang, C. T. Phare, M. C. Shin, M. Zadka, S. P. Roberts, B. Stern, X. Ji, A. Mohanty, O. A. Jimenez Gordillo, U. D. Dave, and M. Lipson, "Large-scale optical phased array using a low-power multi-pass silicon photonic platform," Optica **7**, 3–6 (2020).

19. W. Xu, L. Zhou, L. Lu, and J. Chen, "Aliasing-free optical phased array beam-steering with a plateau envelope," Opt. Express **27**, 3354–3368 (2019).

20. S.-H. Kim, J.-B. You, Y.-G. Ha, G. Kang, D.-S. Lee, H. Yoon, D.-E. Yoo, D.-W. Lee, K. Yu, C.-H. Youn, and H.-H. Park, "Thermo-optic control of the longitudinal radiation angle in a silicon-based optical phased array," Opt. Lett. **44**, 411–414 (2019).

21. P. Wang, G. Luo, Y. Xu, Y. Li, Y. Su, J. Ma, R. Wang, Z. Yang, X. Zhou, Y. Zhang, and J. Pan, "Design and fabrication of a SiN-Si dual-layer optical phased array chip," Photon. Res. **8**, 912–919 (2020).

22. D. N. Hutchison, J. Sun, J. K. Doylend, R. Kumar, J. Heck, W. Kim, C. T. Phare, A. Feshali, and H. Rong, "High-resolution aliasing-free optical beam steering," Optica **3**, 887–890 (2016).

23. L.-M. Leng, Y. Shao, P.-Y. Zhao, G.-F. Tao, S.-N. Zhu, and W. Jiang, "Waveguide superlattice-based optical phased array," Phys. Rev. Appl. **15**, 014019 (2021).

24. S. Chung, M. Nakai, S. Idres, Y. Ni, and H. Hashemi, "19.1 optical phased-array FMCW LiDAR with on-chip calibration," in *IEEE International Solid-State Circuits Conference (ISSCC)* (IEEE, 2021), pp. 286–288.

25. T. Komljenovic and P. Pintus, "On-chip calibration and control of optical phased arrays," Opt. Express **26**, 3199–3210 (2018).

26. J. Shim, J.-B. You, H.-W. Rhee, H. Yoon, S.-H. Kim, K. Yu, and H.-H. Park, "On-chip monitoring of far-field patterns using a planar diffractor in a silicon-based optical phased array," Opt. Lett. **45**, 6058–6061 (2020).

27. H. Zhang, Z. Zhang, C. Peng, and W. Hu, "Phase calibration of on-chip optical phased arrays via interference technique," IEEE Photon. J. **12**, 6600210 (2020).

28. J. Peurifoy, Y. Shen, L. Jing, Y. Yang, F. Cano-Renteria, B. G. DeLacy, J. D. Joannopoulos, M. Tegmark, and M. Soljačić, "Nanophotonic particle simulation and inverse design using artificial neural networks," Sci. Adv. **4**, eaar4206 (2018).

29. J. Carrasquilla and R. G. Melko, "Machine learning phases of matter," Nat. Phys. **13**, 431–434 (2017).

30. J. Liu, D. Zhang, D. Yu, M. Ren, and J. Xu, "Machine learning powered ellipsometry," Light Sci. Appl. **10**, 55 (2021).

31. R. T. Chen and Z. Fu, "Optical true-time delay control systems for wideband phased array antennas," in *Progress in Optics*, E. Wolf, ed. (Elsevier, 2000), pp. 283–359.

32. I. Goodfellow, Y. Bengio, and A. Courville, *Deep Learning* (MIT, 2016).

33. D. Wang, Q. Du, T. Zhou, D. Li, and R. Wilcox, "Stabilization of the 81-channel coherent beam combination using machine learning," Opt. Express **29**, 5694–5709 (2021).

34. R. W. Gerchberg and W. O. Saxton, "Practical algorithm for determination of phase from image and diffraction plane pictures," Optik **35**, 237–246 (1972).

35. J. R. Fienup, "Reconstruction of an object from the modulus of its Fourier transform," Opt. Lett. **3**, 27–29 (1978).

36. N. Streibl, "Phase imaging by the transport equation of intensity," Opt. Commun. **49**, 6–10 (1984).

37. R. Gonsalves, "Phase retrieval and diversity in adaptive optics," Opt. Eng. **21**, 215829 (1982).

38. G. R. Brady and J. R. Fienup, "Nonlinear optimization algorithm for retrieving the full complex pupil function," Opt. Express **14**, 474–486 (2006).

39. S. W. Paine and J. R. Fienup, "Machine learning for improved image-based wavefront sensing," Opt. Lett. **43**, 1235–1238 (2018).

40. A. Sinha, J. Lee, S. Li, and G. Barbastathis, "Lensless computational imaging through deep learning," Optica **4**, 1117–1125 (2017).

41. Y. Nishizaki, M. Valdivia, R. Horisaki, K. Kitaguchi, M. Saito, J. Tanida, and E. Vera, "Deep learning wavefront sensing," Opt. Express **27**, 240–251 (2019).

42. J. Kansky, C. Yu, D. Murphy, S. Shaw, R. Lawrence, and C. Higgs, "Beam control of a 2D polarization maintaining fiber optic phased array with high-fiber count," Proc. SPIE **6306**, 63060G (2006).

43. J. Kennedy and R. Eberhart, "Particle swarm optimization," in *International Conference on Neural Networks (ICNN)* (IEEE, 1995), pp. 1942–1948.